Advanced Two Phase Flow Model for Transient Molten Salt Receiver System Simulation

Christian Schwager[a,*], Robert Flesch[b,1], Peter Schwarzbözl[c], Ulf Herrmann[a] , Cristiano José Teixeira Boura[a]

[a] Solar-Institut Jülich (SIJ) of the Aachen University of Applied Sciences, Heinrich-Mussmann-Str. 5, 52428 Juelich, Germany

[b] German Aerospace Center (DLR), Institute of Solar Research, Prof. Rehm-Strasse 1, 52428 Juelich, Germany

[c] German Aerospace Center (DLR), Institute of Solar Research, Linder Hoehe, 51147 Cologne, Germany

Abstract

In order to realistically predict and optimize the actual performance of a concentrating solar power (CSP) plant sophisticated simulation models and methods are required. This paper presents a detailed dynamic simulation model for a Molten Salt Solar Tower (MST) system, which is capable of simulating transient operation including detailed startup and shutdown procedures including drainage and refill. For appropriate representation of the transient behavior of the receiver as well as replication of local bulk and surface temperatures a discretized receiver model based on a novel homogeneous two-phase (2P) flow modelling approach is implemented in Modelica Dymola®. This allows for reasonable representation of the very different hydraulic and thermal properties of molten salt versus air as well as the transition between both. This dynamic 2P receiver model is embedded in a comprehensive one-dimensional model of a commercial scale MST system and coupled with a transient receiver flux density distribution from raytracing based heliostat field simulation. This enables for detailed process prediction with reasonable computational effort, while providing data such as local salt film and wall temperatures, realistic control behavior as well as net performance of the overall system. Besides a model description, this paper presents some results of a validation as well as the simulation of a complete startup procedure. Finally, a study on numerical simulation performance and grid dependencies is presented and discussed.

Keywords:

1 Introduction

Recently, Concentrated Solar Power (CSP) has developed from an innovative green technology to a growing industry of mayor importance for the global energy transition. Molten Salt Solar Towers (MST) pose the most established and commercially utilized point focusing technology, while achieving the highest yield per occupied land area (Ahmadi et al., 2018). Still, they hold great potential for efficiency improvements and cost reduction. Especially operational efficiency has been

---

∗ Corresponding author: schwager@sij.fh-aachen.de

1 Present address: Schloßhof 11, 71134 Aidlingen, Germany

proven to be challenging, while the receiver system is the most significant cause for unavailability of MST (Kolb, 2011). In the past, freezing has been one of the most demanding issues (Pacheco et al., 2002), whereas today, reliability and lifetime play an increasing role. Hence, more attention to transient behavior (local temperatures, gradients and thermal stresses) and the control systems is needed (Mehos et al., 2020).

Basically, the most critical operational events occur during irregular flux distributions at either a very high or at a low level. The first is obvious, the second is due to low Reynolds numbers during morning and evening hours (Rodriguez-Sanchez et al., 2015). Operation experience from the first commercial MST project Gemasolar led to different startup strategies, under thorough consideration of expected DNI. For instance, in winter, startups are initiated as early as possible because of limited flux in the morning in contrast to fast startups on summer days (Burgaleta et al., 2012). Further, performance limitations due to cloudy conditions are reported, especially during partial shading, which cause decreasing outlet temperatures (García and Calvo, 2012). This is also confirmed by first operation experiences from the NOOR III MST. In order to avoid local hotspots during volatile DNI conditions, the molten salt receiver is operated on a semi fixed mass flow rate, resulting in heavy outlet temperature fluctuations (Relloso, 2019).

In the light of the above, simulation models that are used for performance evaluation of MST need to consider these operational features. However, the commercially available simulation tools usually neglect certain details about the actual limitations of the receiver system they represent, which leads to non-realistic overpredictions of annual yield in the range of 11 % (Relloso and Gutiérrez, 2016). For instance, the dynamic behavior and with that the controllability of a molten salt receiver, depends on not only the temporal but also the spatial variability of the DNI. Neglecting just this, can lead to a yield overprediction around 2 - 4 % (Schwager et al., 2019). Furthermore, allowable flux density (AFD) limits, which were introduced to prevent exceeding of limitations for thermal stresses and maximum salt film temperatures, need to be considered (Vant-Hull, 2002; Sánchez-González et al., 2020).

Current research is therefore designated to improve operational efficiency and availability considering realistic limitations and boundary conditions, for which sophisticated software tools and simulation models are developed. One way to control receiver temperatures is through different aim point strategies. For instance, Belhomme et al. (2013) developed a raytracing based aim point optimization algorithm applying an ant colony optimization metaheuristic. This was later improved by Flesch et al. (2017) and Oberkirsch et al. (2021) reaching a performance that allows to even optimize aiming in cloudy conditions. Meanwhile, García et al. (2018) presented a model predictive aiming control methodology combined with a PI-controlled set point adjustment to prevent cloud induced overshooting

Besides, several approaches have been presented to determine transient receiver flux distributions throughout the day and also during cloud passages (Ahlbrink et al., 2012; Augsburger and Favrat, 2013; Schöttl et al., 2018). With these as input data a dynamic thermal model of the receiver system allow for further predictions about actual performance. The challenge however lies in finding an efficient way of modelling the distributed states.

In this regard, the published absorber tube respectively receiver models range from a simple but fast zero-dimensional steady state absorber tube model (Li et al., 2019) over a dynamic one-dimensional models with vertical and circumferential absorber tube wall discretization (Crespi et al., 2018; Losito et al., 2018) to high resolution FEM and CFD models (Fritsch et al., 2017; Uhlig et al., 2018; Montoya et al., 2019). A common approach for dynamic process simulations is to discretize absorber tubes in numerous elements along the direction of flow, but in only two elements along the circumference. By this, Doupis et al. (2016) and Sani et al. (2018) were able to implement drainable receiver models

82   within a larger system model to simulate filling and draining procedures. However, they did not share
83   any details about the applied two-phase flow modelling, and this two-element discretization
84   approach does not reflect the inhomogeneous flux distribution and the resulting temperature peak
85   on the front tube surface. Hence, Flesch et al. (2016) proposed a similar approach but with an
86   addition crown (max) temperature without introducing more differential equations. This was also
87   adopted by R. Popp et al. (2019), who developed a non-drainable but very efficient dynamic model as
88   basis for a model predictive controller, which allows for controlling the outlet temperature by mass
89   flow adjustments while adhering to fluid film temperature and flux limits (Popp et al., 2021).

90   In the context of developing model predictive assistance for molten salt receivers, a model that
91   realistically represents the dynamic behavior of the whole receiver system during volatile solar
92   conditions and transitions between different states of operation was needed. Local temperatures
93   and transients in the receiver panels need to be represented appropriately to identify violations of
94   operational limits. This demands for an efficient modelling approach to maintain the complex
95   receiver model numerically manageable. The model presented by Flesch et al. (2016) poses a suitable
96   approach except for the two-phase (2P) flow model, which is based on a two-fluid modelling
97   approach. The numerical stability is insufficient for larger simulations including a whole receiver and
98   periphery.

99   Consequently, a novel 2P flow model has been developed and implemented into a comprehensive
100   receiver system model. This novel modeling approach incorporates a simplified homogeneous 2P
101   flow model, which uses half as many partial differential equations as the aforementioned two-fluid
102   modeling approach (three instead of six per state). Due to the resulting improvement of numerical
103   performance, this allowed for including not only a basic mass flow control (like state of the art
104   models) but a process control system that manages the whole receiver system though normal
105   operation as well as startup and shutdown procedures applying numerous controllers in
106   combination. Also, the overall model includes comprehensive periphery according to a commercial
107   receiver system layout. The purpose of introducing this additional complexity is to allow for realistic
108   transient simulations of startup and shutdown procedures in clear and cloudy conditions, thus to
109   minimize the gap between predicted and actual yield in MST systems.

110   This paper provides a detailed description of the novel 2P modeling approach, the absorber tube
111   model as well as basic information about the periphery and system model. This is followed by a
112   validation and discussion of simulation results of a typical startup procedure.

2 Modell Description

2.1 Flow Model

115   In general, 2P modelling can be described as a challenging task. Solving the Navier-Stokes equations
116   for both phases in all details is not manageable for today's computers. Especially, "when one or both
117   of the phases becomes turbulent (as often happens) the magnitude of the challenge becomes truly
118   astronomical" (Brennen, 2005), which is why generally certain simplifications are applied to the
119   Navier-Stokes Equations depending on the application and the regime in which the model is being
120   used. This section presents simplifications suitable for a process model of a solar receiver with
121   vertical tubes, generally operated with a liquid and a gas phase. In this case it is justified to consider
122   liquid and gas phase as a separated flow, which simplifies the problem compared to disperse flow.

123   In this sense, ϕ is introduced as volume fraction and ξ as mass fraction of the respective phase.
124   Consequently, for liquid (molten salt) and gas (air) phase this leads to

$$\phi_\mathrm{L} + \phi_\mathrm{G} = 1 \qquad (2.1)$$

125   and

$$\xi_\mathrm{L} + \xi_\mathrm{G} = 1. \qquad (2.2)$$

126   In order to derive one from the other, the following equations apply:

$$\phi_\mathrm{L} = \frac{\dfrac{\xi_\mathrm{L}}{\rho_\mathrm{L}}}{\dfrac{\xi_\mathrm{L}}{\rho_\mathrm{L}} + \dfrac{\xi_\mathrm{G}}{\rho_\mathrm{G}}} \qquad (2.3)$$

$$\phi_\mathrm{G} = \frac{\dfrac{\xi_\mathrm{G}}{\rho_\mathrm{G}}}{\dfrac{\xi_\mathrm{L}}{\rho_\mathrm{L}} + \dfrac{\xi_\mathrm{G}}{\rho_\mathrm{G}}} \qquad (2.4)$$

$$\xi_\mathrm{L} = \frac{\phi_\mathrm{L}\rho_\mathrm{L}}{\phi_\mathrm{L}\rho_\mathrm{L} + \phi_\mathrm{G}\rho_\mathrm{G}} \qquad (2.5)$$

$$\xi_\mathrm{G} = \frac{\phi_\mathrm{G}\rho_\mathrm{G}}{\phi_\mathrm{L}\rho_\mathrm{L} + \phi_\mathrm{G}\rho_\mathrm{G}} \qquad (2.6)$$

127   with the pure substance densities ρ_L and ρ_G.

128   As usually in system modelling approaches, we will use a one-dimensional modelling approach. The
129   two-phase modelling approaches can be categorized by the level of detail in which the flow fields of
130   the two phases are resolved: In case of a two-fluid model the field variables of velocity and
131   temperature locally differ, which leads to six partial differential equations to be solved. Further,
132   closing approximations for impulse exchange and heat transfer between the phases are required
133   (Scheuerer and Scheuerer, 1992; Vij and Dunn, 1996; Masella et al., 1998; Bauer, 1999; Issa and
134   Kempf, 2003; Brennen, 2005; Akselsen, 2012; Hoffmann et al., 2014).

135   However, in vertical receiver tubes we can assume locally identical velocities and temperatures of
136   the phases and thus eliminate two differential equations. This leads to a homogeneous model, in
137   which the flow is treated like the flow of a single phase (Francke, 2014; van Zwieten et al., 2015). The
138   assumption of the identical velocity would not be valid for sections with horizontal flow, but an
139   accurate representation of the two-phase flow is only necessary in the vertical absorber tubes of the
140   receiver. All non-vertical sections in the considered system are slightly angled for drainability, so that
141   the separation of liquid and gas phase is still given, but the further described heat transfer modelling
142   is not valid in these components. However, since these pipes are insulated and electrically heat
143   traced, the convective heat transfer in these pipes is not relevant. Another limitation of this approach
144   is, that if individual tubes are filled quicker or earlier than others and molten salt would spill over
145   from one into another tube, it would lead to invalid results. Nevertheless, this should be avoided by
146   design and proper operation anyway. In an occurrence like that, the problem could be identified with
147   this simulation model knowing that local temperature values at this particular moment would not be
148   applicable.

149   Accordingly, our homogenous model includes three joint differential equations for conservation of
150   mass, momentum and energy

$$\frac{\partial}{\partial t}(\rho) + \frac{\partial}{\partial x}(\rho u) = 0 \qquad (2.7)$$

$$A\rho \frac{\partial}{\partial t}(u) + A\rho u \frac{\partial}{\partial x}(u) = A\rho g_| - A\frac{\partial}{\partial x}(p) + F_W' \tag{2.8}$$

$$A\frac{\partial}{\partial t}(\rho h) + \frac{\partial}{\partial x}(\rho u h A) = \dot{Q}_W' \tag{2.9}$$

151   plus one additional continuity equation for the liquid phase

$$A\frac{\partial}{\partial t}(\phi_L \rho_L) + \frac{\partial}{\partial x}(\phi_L \rho_L u_L A) = 0. \tag{2.10}$$

152   All substance properties are determined from a mixture of the pure substance properties.

153   Since the time scales on which the flow adapts to pressure changes are much shorter than those of
154   the considered heat tranfer, the flow does not need to be simulated fully dynamically. Hence, the
155   time derivative and the convective term in equation (2.8) can be neglected. The momentum
156   equation is therefore simplified to

$$A\frac{\partial}{\partial x}(p) = \xi_L A\rho g_| + F_W'. \tag{2.11}$$

157   With this simplification it would be unnecessary to solve the total mass balance (2.7) as it is only
158   relevant to resolve local velocity gradients, but it is kept for numerical purposes. The component
159   mass balance (2.10) is solved to get the receiver filling level and the energy equation (2.9) provides
160   the fluid temperature. However, in order to avoid rapid changes in (2.7) during filling, the density is
161   kept nearly independent from the composition (see. section 2.2). In order to account for the
162   different gravitational forces on liquid and gas, the mass fraction of the liquid ξ_L has been added to
163   the geodetic term in equation (2.11), hence switching is off if an element is empty.

164   Regarding the thermal significance of air inside the absorber tubes (with typically $d_I/_{\Delta r} \approx 20$), there
165   are three orders of magnitude between the absolute heat capacity of the tube wall and the air
166   volume inside the tube. Consequently, the influent of stagnant air on the wall temperature is
167   negligible.

2.2   Medium Model

169   In respect to the aforementioned flow model and the associated assumption that the composition
170   has nearly no effect on the density, the differences between volume fraction and mass fraction
171   disappear. Therefore, the substance properties are all defined as a function of temperature T,
172   pressure p and the composition ξ_L. The density is defined as

$$\rho = (1 + (p - p_{ref})(\kappa_L \xi_L + \kappa_G \xi_G) - (T - T_{ref})\beta_L)\rho_{ref} \tag{2.12}$$

173   with an artificial compressibility κ_G, which on the one hand improves numerical stability and on the
174   other hand still guarantees a solution. The artificial heat capacity of the gas is adjusted so that $\rho c_{p,G}$
175   is in the order of magnitude of the real value of air. The isothermal compressibility of the gas poses a
176   trade-off between the requirement that the density should not change too much (because of the
177   assumption $\xi_L = \phi_L$) and the numerical stability/performance, since compressible media perform
178   better in Dymola® than simulations of incompressible media. Furthermore, the specific enthalpy can
179   be described as

$$h = h_{ref} + (T - T_{ref}) \cdot (c_{p,L} \cdot \xi_L + c_{p,G} \cdot \xi_G). \tag{2.13}$$

180   As shown, the dependency on pressure is neglected. The temperature rise due to adiabatic throttling
181   is usually less than 1 K in such a system, which justifies this approximation. This also implies that

182 $u = h$. Moreover, since the specific heat capacity of the molten salt actually varies by only 1.5 %
183 between 290 °C to 565 °C, it is considered constant. Finally, the physical properties are modelled as
184 follows:

$$\lambda = 0.443 + 0.00019 \frac{W}{m\,K^2} \cdot \theta \tag{2.14}$$

185 for the thermal conductivity λ and

$$\mu = 10^{-3} \cdot \left[22.714 + \theta \cdot \left(-0.12 + \theta \cdot \left(2.281 \cdot 10^{-4} + \theta \cdot (-1.474) \cdot 10^{-7}\right)\right)\right] \tag{2.15}$$

186 for the dynamic viscosity μ using $\theta = (T - 273.15\ K)$ as the temperature value in °C. In Table 1 the
187 assumed values for the mentioned properties are listed.

188 Table 1. Assumed properties for homogenous pseudo mixture aligning with literature (Zavoico, 2001)

Reference density	ρ_{ref}	1,949.44 m³/kg
Reference enthalpy	h_{ref}	104,929 J/kg
Specific heat capacity of liquid	$c_{p,L}$	1,516.53 J/(kgK)
Artificial specific heat capacity of gas	$c_{p,G}$	1 J/(kgK)
Isothermal compressibility of liquid	κ_L	1·10⁻¹⁰ 1/Pa
Isothermal compressibility of gas	κ_G	1·10⁻⁷ 1/Pa
Thermal expansion coefficient	β_L	3.262468683·10⁻⁴ 1/K

2.3 Absorber Tube Model

2.3.1 Tube wall

191 The transient heat conduction in a cylindrical body can be described by this partial differential
192 equation (Verein Deutscher Ingenieure, 2013):

$$\frac{\rho c_p}{\lambda} \frac{\partial T}{\partial t} = \frac{1}{r} \frac{\partial}{\partial r}\left(r \frac{\partial T}{\partial r}\right) + \frac{1}{r^2} \frac{\partial^2 T}{\partial \varphi^2} + \frac{\partial^2 T}{\partial z^2} \tag{2.16}$$

193 with cylinder coordinates r, φ and z. Analogue to the modelling approach previously used by Flesch
194 et al. (2016), the absorber tube wall is discretized into a flexible number of elements in the direction
195 of flow, which are circumferentially discretized into a front and a back shell as well as. The radial
196 discretization is represented by three temperatures (compare Fig. 1). The outer and inner surface
197 temperature $T_{O,j}$ and $T_{I,j}$ are determined by the respective boundary conditions. The core
198 temperature $T_{C,j}$ is defined by a time differential considering the heat capacity of the wall. Based on
199 this and equation (2.16) the core temperature $T_{C,j}$ can be derived from

$$V_j \rho c_p \frac{\partial T_{C,j}}{\partial t} = \pi \cdot \Delta z \cdot \lambda \cdot \frac{T_{O,j} - T_{C,j}}{\ln\left(\frac{d_O}{d_C}\right)} - \pi \cdot \Delta z \cdot \lambda \cdot \frac{T_{C,j} - T_{I,j}}{\ln\left(\frac{d_C}{d_I}\right)}$$
$$+ A_{FB} \cdot \frac{\lambda}{r_C} \cdot \frac{\left(T_{FB,j} - T_{C,j}\right)}{\pi} + A_Q \cdot \lambda \cdot \frac{T_{C,j+1} - T_{C,j}}{\Delta z} - A_Q \cdot \lambda \cdot \frac{T_{C,j} - T_{C,j-1}}{\Delta z} \tag{2.17}$$

200 with the volume of the discrete half shell of element j (vertical discretization)

$$V_j = A_Q \cdot \Delta z = \frac{1}{2} \cdot \frac{\pi\left(d_O^2 - d_I^2\right)}{4} \cdot \Delta z \tag{2.18}$$

201 and the contact area between front and back shell

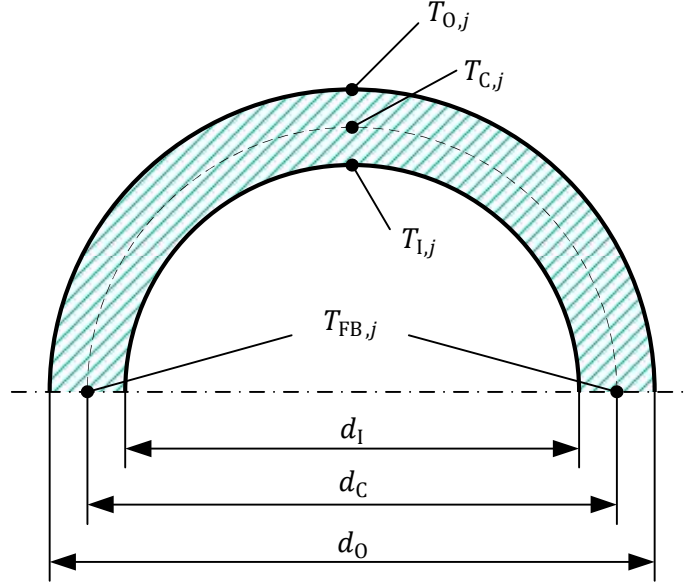$$A_{\mathrm{FB}} = (d_{\mathrm{O}} - d_{\mathrm{I}}) \cdot \Delta z. \tag{2.19}$$

Fig. 1. Discrete temperatures of a tube shell element

Moreover, the boundary conditions for the outer surface temperatures of the front shell $T_{\mathrm{F,O},j}$ follow as

$$\dot{Q}_{\mathrm{abs},j} - \dot{Q}_{\mathrm{rad},j}(T_{\mathrm{O},j}) - \dot{Q}_{\mathrm{conv},j}(T_{\mathrm{F,O},j}) = \pi \cdot \Delta z \cdot \lambda \cdot \frac{T_{\mathrm{F,O},j} - T_{\mathrm{F,C},j}}{\ln\left(\frac{d_{\mathrm{O}}}{d_{\mathrm{C}}}\right)}, \tag{2.20}$$

whereas the corresponding equation for the back shell can be set to zero, considering that heat losses through the backside of the tube can be neglected due to adequate insulation. For the inner surface (film) temperature, the following equation applies for both, front and back shell:

$$\pi \cdot \Delta z \cdot \lambda \cdot \frac{T_{\mathrm{C},j} - T_{\mathrm{I},j}}{\ln\left(\frac{d_{\mathrm{C}}}{d_{\mathrm{I}}}\right)} = \dot{Q}_{\mathrm{fluid},j}(T_{\mathrm{I},j}) \tag{2.21}$$

In order to further simplify the tube wall model, the heat flow rates in the tube wall are compared with each other. Based on typical temperature gradients the dominant heat flow, which is the one in radial direction through the front shell, lies in the order of 10^4 W, while the thermal conduction in (vertical) flow direction is approximately 10^{-2} W and can consequently be neglected. The heat flow between front and back shell reaches approximately 10^2 W at normal operation and is therefore less significant as well. However, when the empty tubes are preheated (during startup) the flux density is much lower and the convective heat flow into the fluid (air) nearly zero so that the front-to-back heat flow becomes dominant (essential mechanism for preheating the whole tube). Besides, the designated temperature sensors are installed on the backside of the absorber tubes. In this case the vertical gradients are even smaller than during normal operation, so that the vertical heat flow is still insignificant. Consequently, equation (2.17) is reduced to

$$V_j \rho c_{\mathrm{p}} \frac{\partial T_{\mathrm{F,C},j}}{\partial t} = \pi \cdot \Delta z \cdot \lambda \cdot \frac{T_{\mathrm{F,O},j} - T_{\mathrm{F,C},j}}{\ln\left(\frac{d_{\mathrm{O}}}{d_{\mathrm{C}}}\right)} - \pi \cdot \Delta z \cdot \lambda \cdot \frac{T_{\mathrm{F,C},j} - T_{\mathrm{F,I},j}}{\ln\left(\frac{d_{\mathrm{O}}}{d_{\mathrm{C}}}\right)} + A_{\mathrm{FB}} \cdot \frac{\lambda}{r_{\mathrm{C}}} \cdot \frac{\left(T_{\mathrm{FB},j} - T_{\mathrm{F,C},j}\right)}{\pi} \tag{2.22}$$

for the front shell and

$$V_j \rho c_\text{p} \frac{\partial T_{\text{B,C},j}}{\partial t} = -\pi \cdot \Delta z \cdot \lambda \cdot \frac{T_{\text{B,C},j} - T_{\text{B,I},j}}{\ln\left(\frac{d_\text{c}}{d_\text{i}}\right)} + A_\text{FB} \cdot \frac{\lambda}{r_\text{c}} \cdot \frac{\left(T_{\text{FB},j} - T_{\text{B,C},j}\right)}{\pi} \tag{2.23}$$

221   for the back shell, while applying the same boundary conditions as above.

222   **Crown temperatures**

223   The above described approach for the receiver tubes only considers two average temperatures (front

224   and back) along the circumference of the absorber tube. In reality the nearly parallel radiation from

225   the heliostat field is perpendicular to the tube surface only at the crown, whereas the incident angle

226   and therefore the local flux density decreases towards the sides. As a result, the temperature

227   distribution in the front element is highly inhomogeneous. The calculated mean temperature cannot

228   reflect this circumferential profile and is only valid for the energy balance of each element. In terms

229   of operational limits, the maximum temperatures at the pipe crown are of special interest. Instead of

230   increasing the number of circumferential discrete elements, which would drastically increase the

231   complexity and therefore compromise the computational performance of the model, a different

232   approach is implemented posing only a few additional algebraic equations.

233   Recently, Flesch et al. (Flesch et al., 2017) proposed the following: since at the crown of the absorber

234   tube the temperature gradient $\partial T / \partial \varphi \approx 0$ due to symmetry, the circumferential heat flow in this

235   point is neglected, resulting in two algebraic equations for the associated outer and inner surface

236   temperatures $T_{\text{Cr,O},j}$ and $T_{\text{Cr,I},j}$. However, the circumferential heat flow actually correlates to

237     $\partial^2 T / \partial \varphi^2$, which is less than zero and can be significant – especially at low mass flow rates.

238   Therefore, an improved approach is based on an infinitely small (in circumferential direction) sub-

239   element at the crown of the tube as shown in Fig. 2. Its radial and axial extend is the same as the

240   discrete half shell element of the tube model. A steady state energy balance for this segment is

241   described as

$$0 = \frac{T_{\text{Cr,O},j} - T_{\text{Cr,C},j}}{\ln\left(\frac{d_\text{O}}{d_\text{C}}\right)} - \frac{T_{\text{Cr,C},j} - T_{\text{Cr,I},j}}{\ln\left(\frac{d_\text{C}}{d_\text{I}}\right)} + \frac{2\Delta r}{d_\text{C}} \frac{\partial^2 T}{\partial \varphi^2}\Bigg|_{\varphi=0} \tag{2.24}$$

242   with three additional temperatures $T_{\text{Cr,O},j}$, $T_{\text{Cr,C},j}$ and $T_{\text{Cr,I},j}$ at the crown.
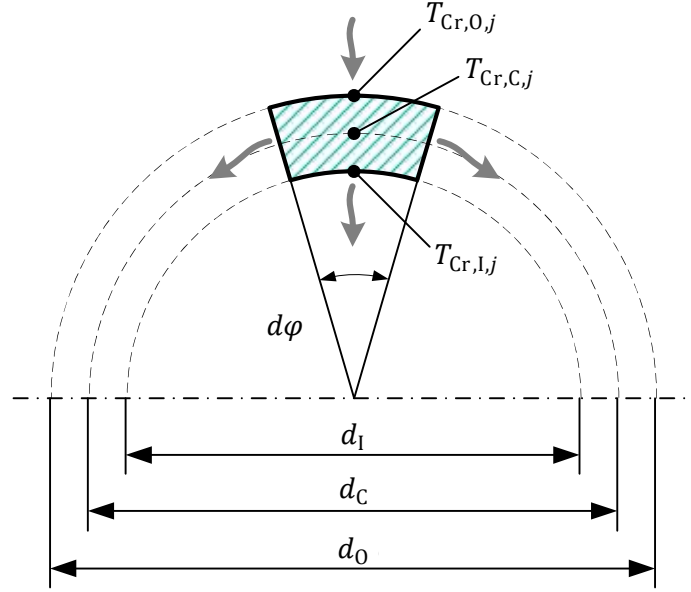
Fig. 2. Infinitely small tube wall element with crown temperatures

In addition to equation (2.24), the outer surface boundary condition is

$$\lambda \frac{T_{\text{Cr,O},j} - T_{\text{Cr,C},j}}{\ln\left(\frac{d_\text{O}}{d_\text{C}}\right)} = \frac{d_\text{O}}{2} \cdot \left(\dot{q}''_{\text{abs},j} - \dot{q}''_{\text{rad},j}(T_{\text{Cr,O},j}) - \dot{q}''_{\text{conv},j}(T_{\text{Cr,O},j}) \right) \tag{2.25}$$

and the absorbed flux density (area specific heat flow rate)

$$\dot{q}''_{\text{abs},j} = \alpha \cdot \dot{q}''_{\text{flux},j} \tag{2.26}$$

without any view factor, since this infinitely small segment only sees the ambient. Accordingly, the radiation losses are determined by

$$\dot{q}''_{\text{rad},j} = \varepsilon \cdot \sigma \cdot \left(T_{\text{Cr,O},j}{}^4 - T_\infty{}^4 \right) \tag{2.27}$$

and convective heat losses by

$$\dot{q}''_{\text{conv},j} = \alpha_{\text{conv,O}} \cdot \left(T_{\text{Cr,O},j} - T_\infty \right). \tag{2.28}$$

Moreover, the inner surface boundary condition follows

$$\lambda \frac{T_{\text{Cr,C},j} - T_{\text{Cr,I},j}}{\ln\left(\frac{d_\text{C}}{d_\text{I}}\right)} = \frac{d_\text{I}}{2} \cdot \dot{q}''_{\text{fluid},j}(T_{\text{Cr,I},j}, T_{\text{fluid},j}) \tag{2.29}$$

applying the same convective heat transfer coefficient $\alpha_{\text{conv,I},j}$ as in equation (2.38).

Lastly, there is the unknown $\partial^2 T / \partial \varphi^2$ in equation (2.24). To avoid introducing more differential equations, an approximation for $T(\varphi)$ is required. Since the tube is irradiated only perpendicular to the crown, the temperature profile is symmetric with a maximum point in the center ($\varphi = 0$) and progressive slopes to the edges. So, a parabola seems appropriate as a functional approach:

$$T_{\text{F,C},j}(\varphi) = T_{\text{Cr,C},j} + \left(T_{\text{FB},j} - T_{\text{Cr,C},j} \right) \left(\frac{2\varphi}{\pi} \right)^2 \tag{2.30}$$

9

$$\Rightarrow \left.\frac{\partial^2 T_{F,C,j}}{\partial \varphi^2}\right|_{\varphi=0} = \frac{8}{\pi^2}\left(T_{FB,j} - T_{Cr,C,j}\right) \approx 0.81 \cdot \left(T_{FB,j} - T_{Cr,C,j}\right) \tag{2.31}$$

256 Alternatively, with a cosine approach the factor 0.81 would be 1.0 instead, resulting in a greater
257 circumferential heat flow, hence lower crown temperature. This means, the parabola function serves
258 a more conservative approach. Finally, the equations (2.24), (2.25) and (2.29) pose an equation
259 system, from which the three crown temperatures can be determined, while the number of
260 differential equations is kept low. The error by assuming a steady state energy balance in (2.24)
261 should be negligible, since the dynamics are well represented in the finite element model of the half
262 shell. It would only be necessary to make this equation transient, if the aforementioned
263 circumferential temperature profile would significantly change during operation. This is not
264 expected, since it only depends on a fixed geometry.

2.3.2 Internal radiation

266 In addition to thermal conduction in the tube wall, radiation exchange in the empty elements
267 between the front and the back shell is considered. In the following, the inner surface area of the
268 tube shell is labelled A_I and the projected area A_d. The front shell is indexed F, the back shell B.
269 Accordingly, the surface brightness of the front shell inner surfaces is

$$A_I \cdot \dot{q}_F'' = \varepsilon A_I \cdot \dot{q}_{F,\sigma}'' + \rho A_I \Phi_{F\to F} \cdot \dot{q}_F'' + \rho A_I \Phi_{B\to F} \cdot \dot{q}_B'' \tag{2.32}$$

270 with the emitted radiation $\varepsilon A_I \cdot \dot{q}_{F,\sigma}'' = \varepsilon A_I \cdot \sigma T_{F,I}^4$, the reflection of the self-irradiation $\rho A_I \Phi_{F\to F} \cdot \dot{q}_F''$
271 and the reflection of the radiation coming from the back shell $\rho A_I \Phi_{B\to F} \cdot \dot{q}_B''$. In this context the view
272 factors can be derived as follows

$$\Phi_{F\to d} A_I = \Phi_{d\to F} A_d \quad , \quad \Phi_{d\to F} = 1 - \Phi_{d\to d} = 1 \tag{2.33}$$

$$\Rightarrow \Phi_{F\to d} = \frac{A_d}{A_I} = \frac{2}{\pi} = \Phi_{F\to B} = \Phi_{B\to F} \tag{2.34}$$

$$\Phi_{F\to F} = 1 - \Phi_{F\to B}. \tag{2.35}$$

273 Combining equation (2.32) with an analogue equation for the back shell concludes to

$$\dot{q}_F'' = \frac{(1 - \rho\Phi_{F\to F})\varepsilon \cdot \dot{q}_{F,\sigma}'' + \rho\Phi_{F\to B}\varepsilon \cdot \dot{q}_{B,\sigma}''}{(1 - \rho\Phi_{F\to F})^2 - (\rho\Phi_{F\to B})^2}. \tag{2.36}$$

274 Based on this, the net radiative heat exchange between front and back follows

$$\begin{aligned}
\Delta\dot{Q}_{rad,FB} = A_I\Phi_{F\to B}(\dot{q}_F'' - \dot{q}_B'') &= A_I\left(\dot{q}_{F,\sigma}'' - \dot{q}_{B,\sigma}''\right)\frac{(1 - \rho\Phi_{F\to F})\varepsilon - \rho\Phi_{F\to B}\varepsilon}{(1 - \rho\Phi_{F\to F})^2 - (\rho\Phi_{F\to B})^2} \\
&= A_I\varepsilon\sigma\left(T_{F,I}^4 - T_{B,I}^4\right)\frac{1}{\left(1 - \frac{4}{\pi}\right)\varepsilon + \frac{4}{\pi}}.
\end{aligned} \tag{2.37}$$

275 In addition, this radiative heat flow rate is set to zero when the tube is filled with molten salt. Even
276 though the transmissivity of molten salt is greater than zero, this radiative head exchange is then
277 insignificant in comparison to the convective heat transfer between shell and fluid.

2.3.3 Heat transfer into the fluid

279 In order to complete equation (2.21), the heat transfer from an absorber tube half shell element into
280 the fluid is modelled as

$$\dot{Q}_{\text{fluid},j}\left(T_{\text{I},j}\right) = \alpha_{\text{conv,I},j} \cdot \frac{\pi d_{\text{I}}}{2} \Delta z \cdot \left(T_{\text{I}} - T_{\text{fluid},j}\right) \tag{2.38}$$

with the convective heat transfer coefficient derived from

$$Nu_{\text{I},j} = \frac{\alpha_{\text{conv,I},j} \cdot d_{\text{I}}}{\lambda_j}. \tag{2.39}$$

For the Nusselt number two different correlations for laminar and turbulent flow are implemented based on general correlations for a constant heat flux boundary (Verein Deutscher Ingenieure, 2013). The modified laminar Nusselt number follows

$$Nu_{\text{lam},j} = \left(\left(Nu_1\right)^3 + 1 + \left(Nu_{2,j} - 1\right)^3 + \left(Nu_{3,j}\right)^3 + \left(Nu_{\text{fill},j}\right)^3\right)^{1/3} \tag{2.40}$$

with

$$Nu_1 = 4.364 \tag{2.41}$$

$$Nu_{2,j} = 1.302 \cdot \left(Re_j \, Pr_j \, \frac{d_{\text{I}}}{z_j}\right)^{1/3}. \tag{2.42}$$

$$Nu_{3,j} = 0.462 \cdot Pr_j^{1/3} \left(Re_j \, \frac{d_{\text{I}}}{z_j}\right)^{1/2}. \tag{2.43}$$

In Addition, $Nu_{\text{fill},j}$ accounts for increased heat transfer during filling right below the rising liquid surface due to radial fluid flow (in the not yet developed flow). Based on the results from Flesch et al. (Flesch et al., 2016) it is modelled as follows

$$Nu_{\text{fill},j} = 0.822 \cdot \left(Re_j \, Pr_j \, \frac{d_{\text{I}}}{\Delta z^*}\right)^{0,434}, \tag{2.44}$$

where Δz^* represents the distance between the aforementioned liquid surface and the center of the element j. However, this approach is only valid under constant flow rate. In case of turbulent flow, the Nusselt number conventionally follows

$$Nu_{\text{turb},j} = \frac{\left(\xi_j^*/8\right) Re_j \, Pr_j}{1 + 12.7\sqrt{\xi_j^*/8}\left(Pr_j^{2/3} - 1\right)} \cdot \left(1 + \frac{1}{3} \cdot \left(\frac{d_{\text{I}}}{z_j}\right)^{2/3}\right) \tag{2.45}$$

with

$$\xi_j^* = \left(1.8 \cdot \log\left(Re_j\right) - 1.5\right)^{-2}. \tag{2.46}$$

In the range $Re_j = 2300 \ldots 10000$ the model performs a smooth transition between $Nu_{\text{lam},j}$ and $Nu_{\text{turb},j}$.

2.3.4 Heat input and losses

The absorbed heat flow $\dot{Q}_{\text{abs},j}$ in equation (2.20) is calculated according to

$$\dot{Q}_{\text{abs},j} = \alpha \cdot d_{\text{O}} \cdot \Delta z \cdot \dot{q}_{\text{flux}}''. \tag{2.47}$$

297 The projected surface area of a tube serves as the effective area, since the incidence of the
298 concentrated solar flux can be assumed as nearly parallel. This accounts for the reduction of the flux
299 density on the edge of the tube due to the cosine effect.

300 For calculating radiative heat losses, the radiative heat exchange between adjacent tubes need to be
301 considered. The corresponding view factor can be determined from (Verein Deutscher Ingenieure,
302 2013):

$$\Phi_{\mathrm{O}\to\mathrm{adj}} = \frac{1}{\pi}\left[\pi + \sqrt{\left(2+\frac{2s}{d_\mathrm{o}}\right)^2 - 4} - \left(2+\frac{2s}{d_\mathrm{o}}\right) - 2\arccos\left(\frac{2}{2+\frac{2s}{d_\mathrm{o}}}\right)\right], \tag{2.48}$$

303 which for thin walled tubes ($s \ll d_o$) is approximately $\Phi_{\mathrm{O}\to\mathrm{adj}} = 1 - \frac{2}{\pi}$. Assuming that the
304 temperature differences between adjacent tubes are small and the absorptivity high, only the
305 radiation into the ambient needs to be considered with the corresponding view factor

$$\Phi_{O\to\infty} = 1 - \Phi_{\mathrm{O}\to\mathrm{adj}} = \frac{2}{\pi}. \tag{2.49}$$

306   Consequently, the radiative heat loss of a tube element can be modelled as

$$\dot{Q}_{\mathrm{rad},j}\left(T_{\mathrm{F,O},j}\right) = d_\mathrm{O} \cdot \Delta z \cdot \varepsilon\sigma\left(T_{\mathrm{F,O},j}^4 - T_\infty^4\right). \tag{2.50}$$

307 Moreover, the convective losses can be determined by

$$\dot{Q}_{\mathrm{conv},j}\left(T_{\mathrm{F,O},j}\right) = d_\mathrm{O} \cdot \Delta z \cdot \alpha_{\mathrm{conv,O}}\left(T_{\mathrm{F,O},j} - T_\infty\right). \tag{2.51}$$

308 Applying the real surface area $\frac{\pi}{2}d_\mathrm{O}\Delta z$ would significantly overestimate the convective losses, due to
309 a cavity effect in the corner between two adjacent tubes. In this sense, an appropriate α_{conv}
310 correlation for cross flow cylinders (Verein Deutscher Ingenieure, 2013) can be used.

311 Generally, for high temperature solar receivers convective losses are significantly lower than
312 radiative losses. However, in the lower temperature range, especially during startup, convection is
313 more relevant.

314 **2.4 Receiver Panel Model**
315 Based on the above described absorber tube model, a receiver panel model has been developed
316 according to a typical external molten salt receiver design. Similar to the frequently discussed Solar
317 Two design, one panel is comprised of a bottom and a top header connected to a bundle of adjacent
318 absorber tubes. Accordingly, a dynamic model of a receiver panel is implemented as depicted in Fig.
319 3. The central component represents the irradiated portion of the absorber tubes, whereas the
320 connected pipe components account for non-radiated parts of the tubes. Assuming that adjacent
321 tubes in parallel flow have similar states (at the same height), the model can calculate a reduced
322 number of tubes per panel to enhance the computational performance. Independently from that the
323 discretization in flow direction is adjustable as well. The components that connect the absorber tube
324 assembly to the headers are called multipliers and convert the flow, as to ensure the mass flow rates
325 in the headers and therefore the inlet and outlet of the panel correspond to the real number of
326 absorber tubes. The header model poses a lumped volume model with a temperature-controlled
327 heat tracing considering thermal capacities and resistances of header wall and insulation.
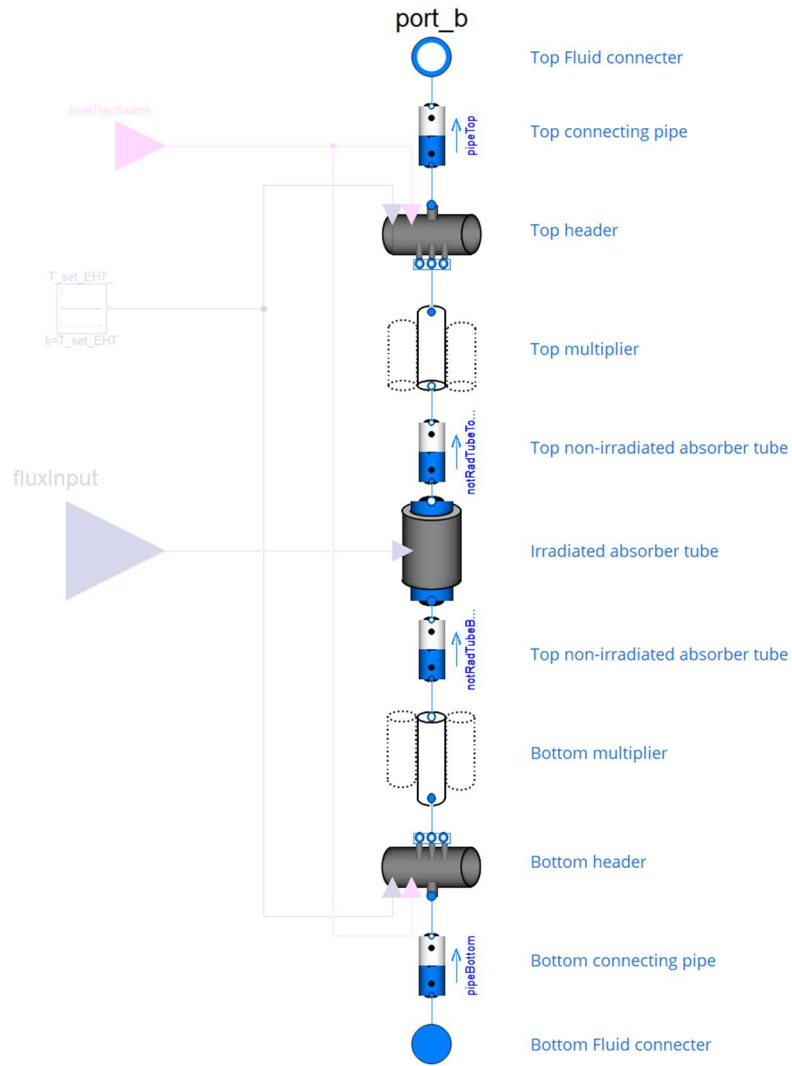
port_b

Top Fluid connecter

Top connecting pipe

Top header

Top multiplier

Top non-irradiated absorber tube

Irradiated absorber tube

Top non-irradiated absorber tube

Bottom multiplier

Bottom header

Bottom connecting pipe

Bottom Fluid connecter

fluxInput

heatTracSwitch

T_set_EHT

k=T_set_EHT

328

329   Fig. 3. Diagram view of the receiver panel model in Dymola®

2.5   Drainable Receiver Model

331 The receiver design considered in this work originates from General Electric (GE) and relates to the
332 one presented by ALSTOM (Das et al., 2015). Similar to other commercial designs, this receiver is
333 subdivided into two independently operated parallel flow paths. The presented model, which is
334 visualized in Fig. 4, comprises all components that exist for each flow path separately. The top left
335 corner shows the inlet, which is connected to the inlet vessel of the receiver system. From there the
336 salt flows through the main control valve and then either through an isolation valve to the receiver
337 panels or down into the main drain line, which acts as a fill, drain or bypass line.

338
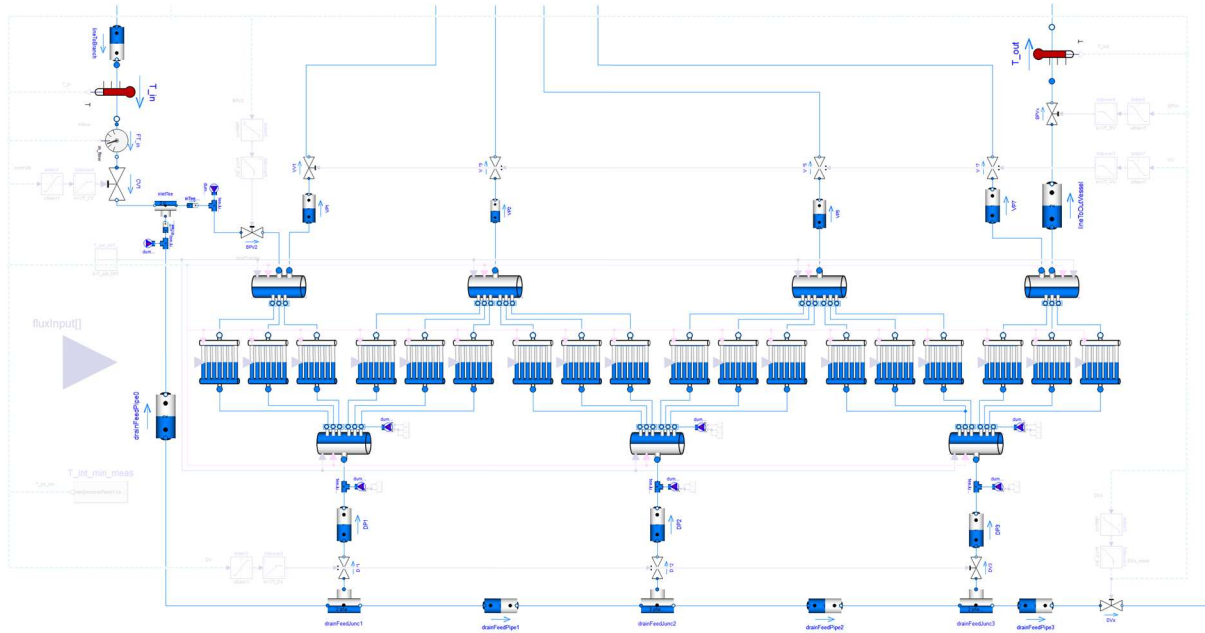
Fig. 4. Diagram view of the receiver flow path model in Dymola®

340   The main (serpentine) flow of the flow path, located in the middle, is realized by three downwards
341   and three upwards passes each consisting of multiple panels in parallel. Since the number of panels
342   per pass in the GE design is classified, these data have been falsified in this illustration. Furthermore,
343   panels in one pass are jointed together by top and bottom manifolds, which also act as
344   interconnecting piping between two passes. These manifolds are modelled in the same way as the
345   aforementioned headers. It is worth mentioning, that they both, header and manifold models,
346   consider the non-diffusive transport of composition, i.e. salt only exits the top connectors if the
347   volume is almost completely filled and air only exits the bottom connectors if the volume is nearly
348   empty. This is important to accurately determine flood and drainage durations. Finally, the top right
349   corner indicates the outlet of the serpentine flow with another isolation valve.

350   To serve the purpose of simulating startup and shutdown procedures, this flow path model also
351   includes drain and vent periphery. During flooding the aforementioned main drain line guides the
352   molten salt to the bottom manifold through drain valves, while the displaced air in the receiver exits
353   through four vent valves on top of the upper manifolds. In the bottom right corner, the main drain
354   valve leads to the downcomer line of the receiver system.

355   All valves that are implemented in this model consider individual actuation speed and leakage.
356   Especially, the large size isolation valves actuate significantly slower and thus affect control
357   performance during transitions. The leakage of valves is not considered as realistic representation of
358   the physical components but it improves the numeric stability and performance of the simulation
359   model, due to the avoidance of zero mass flow rates. However, these leakages might cause
360   undesired results, since they allow molten salt to flow into the empty manifolds and receiver panels
361   before any drain valves are open. To counteract this premature filling of the receiver, mass flow
362   sources and sinks are connected to the lower manifolds, which create a slight flush current of air
363   between manifold and drain valve. Since it flows opposite direction and is greater than the leakage
364   flow, this prevents any liquid from rising into the manifold. Furthermore, during drainage with
365   pressurized air, it is possible that small amounts of air leak from the empty panels through the
366   isolation into the main drain line creating unnecessary difficulties for the solver. For this reason,
367   there is also a slight flush current of molten salt opposing the air leakage. These flush currents are in
368   the order of approx. 0.5 % of nominal flow and have no significant impact on the relevant simulation

369 results of the receiver system, but increase the numerical stability and performance of the simulation
370 model.

371 The intercept flux density distribution on the receiver surface is given to the model in an array, which
372 corresponds to the number of discrete elements in vertical direction and along the circumference of
373 the cylindrical receiver. These flux density arrays are obtained from the raytracing software STRAL
374 (Belhomme et al., 2009; Ahlbrink et al., 2012) and transmitted to the Dymola® Simulation either
375 through the co-simulation tool TISC or by a pre-processed input file (compare (Flesch et al., 2018)).
376 By linear interpolation between time steps, the physical model is simulated with a continuously
377 changing flux density array instead of stepwise changes.

2.6 Top Level Model – Receiver system, Thermal Storage and Process Control System

380 Basic background information about typical commercial receiver designs is provided in the available
381 literature (Zavoico, 2001; Kolb, 2011; Das et al., 2015; Rodriguez-Sanchez et al., 2015) as well as
382 about the operation of such a system (Pacheco et al., 2002; Burgaleta et al., 2012; Relloso and García,
383 2015; Relloso and Gutiérrez, 2016). Accordingly, Fig. 5 illustrates the top-level simulation model, in
384 which the above described receiver model is embedded for two-phase simulations. It includes the
385 entire receiver system and the thermal storage system. It is designed for nominal 650 MW$_{th}$ receiver
386 output and nominal storage temperatures of 290 °C respectively 565 °C.

387
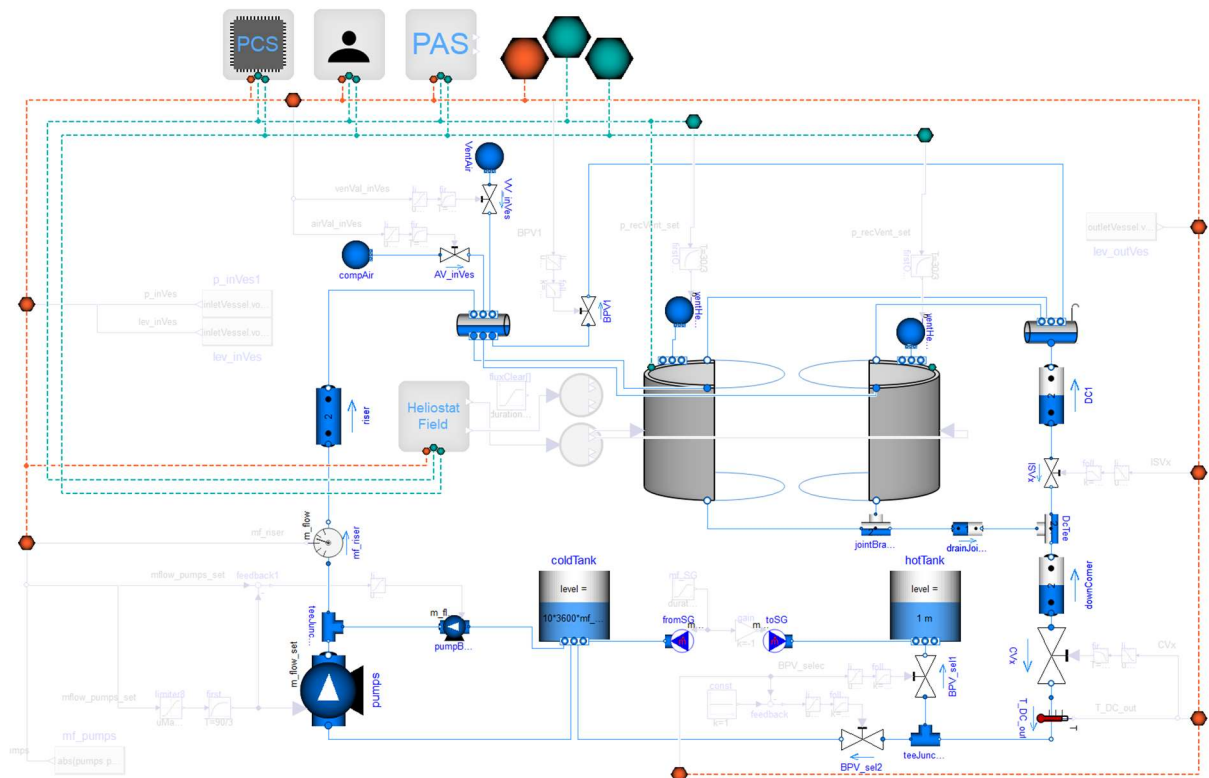
388 Fig. 5. Top level diagram view of the dynamic simulation model

389 Starting at the cold storage tank, the molten salt is fed by the receiver pumps up through the riser
390 into the pressurized inlet vessel. From there the flow splits up into the two flow paths (compare Fig.
391 4) and exists through the top outlet ports into the non-pressurized outlet vessel during normal
392 operation or through the drain ports directly into the downcomer during transitions. After the
393 downcomer, the molten salt can either flow into the hot storage tank or being recycled into the cold
394 storage tank. The heliostat field is represented by a component, which acts as an interface to the

395 raytracing software STRAL and controls normal or preheat flux depending on the active operation
396 mode.

397 The process control system (PCS) includes all control units running the system. For instance, the inlet
398 vessel level is controlled by the speed of the pumps and its ullage pressure is maintained by venting
399 or pressurizing the vessel with compressed air via two control valves on the top. The outlet vessel
400 level, on the other hand, is controlled by adjusting a control valve at the lower end of the
401 downcomer. Moreover, the two parallel receiver mass flow rates are controlled by designated flow
402 path controllers. In order to achieve constant outlet temperatures, each flow path controller applies
403 a clear-sky mass flow controller or a feedback and feedforward loop combination as used at the Solar
404 Two molten test plant (Pacheco et al., 2002). Lastly, the flow selection station decides into which
405 storage tank the down coming mass flow runs depending on the measured temperature. Since the
406 steam generator (SG) return flow can affect the molten salt temperature in the cold tank and
407 therefore the receiver performance, two prescribed mass flow boundaries represent the molten salt
408 exchange with the SG considering a constant return temperature.

409 Furthermore, the PCS includes a state-machine-based algorithm (using the StateGraph2 library) to
410 conduct transitions between different operating modes, which are set by the human operator. This
411 human operator is supposed to represent the typical behavior of a real operator and changes set
412 values for operating modes based on measurement signals from the bus system and a predefined
413 protocol.

3 Validation

415 Since the main novelty of the presented simulation model lies in the two-phase modelling approach
416 and the crown temperature approximation, the following validation highlights these features for a
417 single absorber tube. For better comparability, this validation references to the same CFD simulation
418 data as Flesch et al. (2016) and Losito et al. (2018). First, local tube wall temperatures are examined
419 in a steady state simulation. For this purpose, both simulations were conducted with the same
420 homogeneous solar flux (related to aperture area, not tube surface) and the same mass flow rate
421 inside the tubes. As a result, Fig. 6 shows the circumferential temperature profile at three different
422 heights of the absorber tube. For both, CFD and Dymola, the resulting temperatures on the inner
423 (black) and outer (green) surface of the absorber tube wall are plotted along the circumference. On
424 the back shell (90° to 180°), the CFD data show a nearly even temperature distribution, which agrees
425 with the Dymola model. At the front shell, the CFD data reveal a great temperature difference
426 between the edges (±90°) and the crown (0°C) of approx. 55 K on the inner and 80 K on the outer
427 surface, which confirms that only one mean temperature for the front shell element alone is not
428 sufficient. However, the crown temperatures, which the Dymola model determines as described in
429 section 2.3.1 meet the CFD results with 4 to 5 K overestimation and therefore hold as a slightly
430 conservative approximation.

431
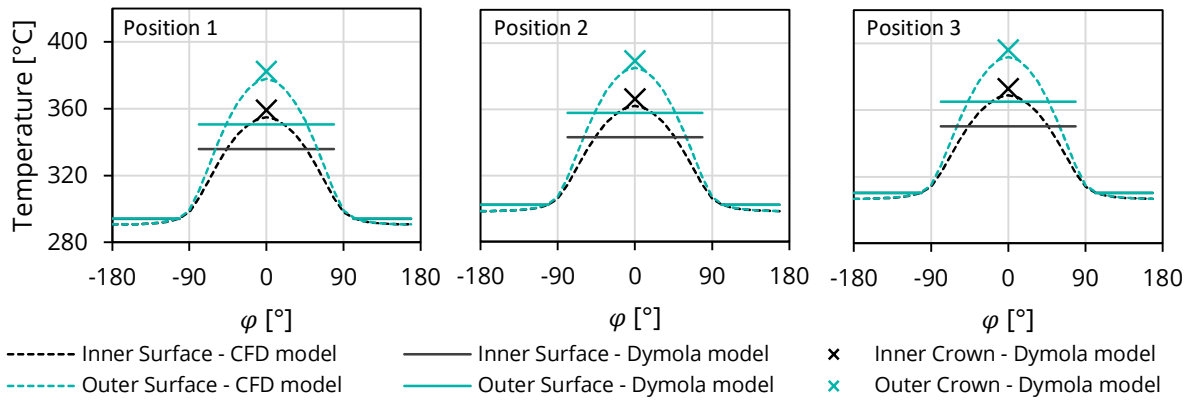
Fig. 6. Circumferential tube wall temperature distribution at three different heights in the Dymola model versus the CFD model

Furthermore, the two-phase modelling is validated with CFD simulations of the single absorber tube being filled with a constant mass flow rate after it has been preheated under constant solar flux and has reached a steady state. Even though this homogeneous model consists of significantly less differential equations than the two fluid model by Flesch et al. (Flesch et al., 2016), it still provides a well representation of the hydraulic and thermal behavior during filling. In Fig. 7 we can observe the course of the molten salt level and the inlet pressure, which results from the geostatic pressure and friction in the filled elements. The graphs of the CFD and Dymola® simulations are hardly distinguishable and deviate by less than 0.2 %.
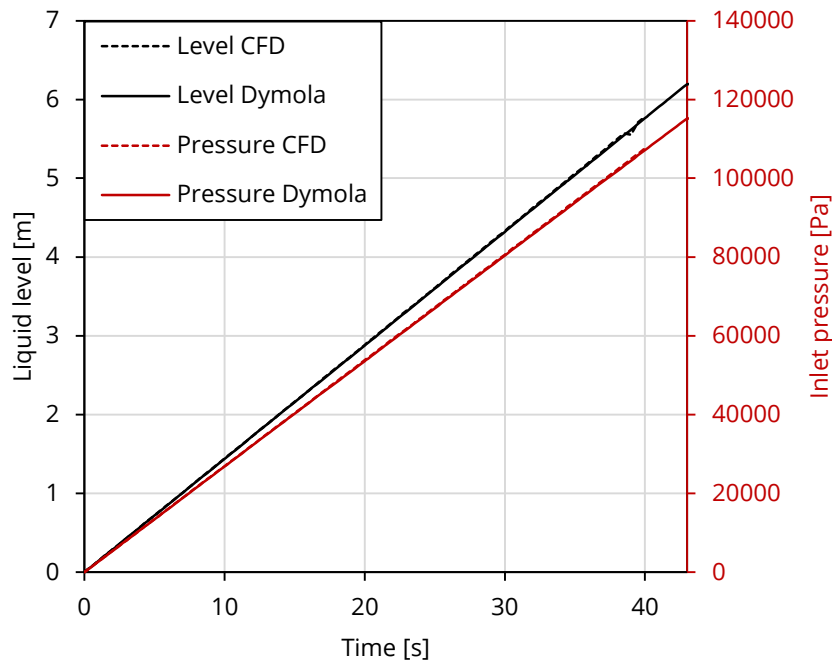
Fig. 7. Course of molten salt level and inlet pressure during filling

Finally, for a validation of the effect of the changing convective heat transfer from the tube wall into the fluid (air and molten salt) during filling (compare section 2.3.3) Fig. 8 depicts the front and backside wall temperatures during a filling simulation at two different heights. It confirms that this homogeneous 2P model represents the transient filling behavior of the preheated absorber tube quite well. The most significant deviation lies in the temperature difference between tube front and

17

450 back site. The higher local flux density at the crown causes the temperature to decrease towards the
451 edges and therefore to be lower on the backside than on the front side, even though the backside is
452 considered adiabatic. Since the Dymola® model only simulates two circumferential elements (front
453 and back) it does not consider this circumferential flux gradient within the front shell element.
454 Hence, in the Dymola® simulation the front and back site temperature are equal until the filling
455 starts. A difference between front and back site temperature develops as soon as convection starts
456 inside the tube. Then the heat flow from the back shell into the fluid causes a front-to-back
457 temperature difference, which seems to converge to the same level as in the CFD model, as the
458 trends in Fig. 8 indicate.

459
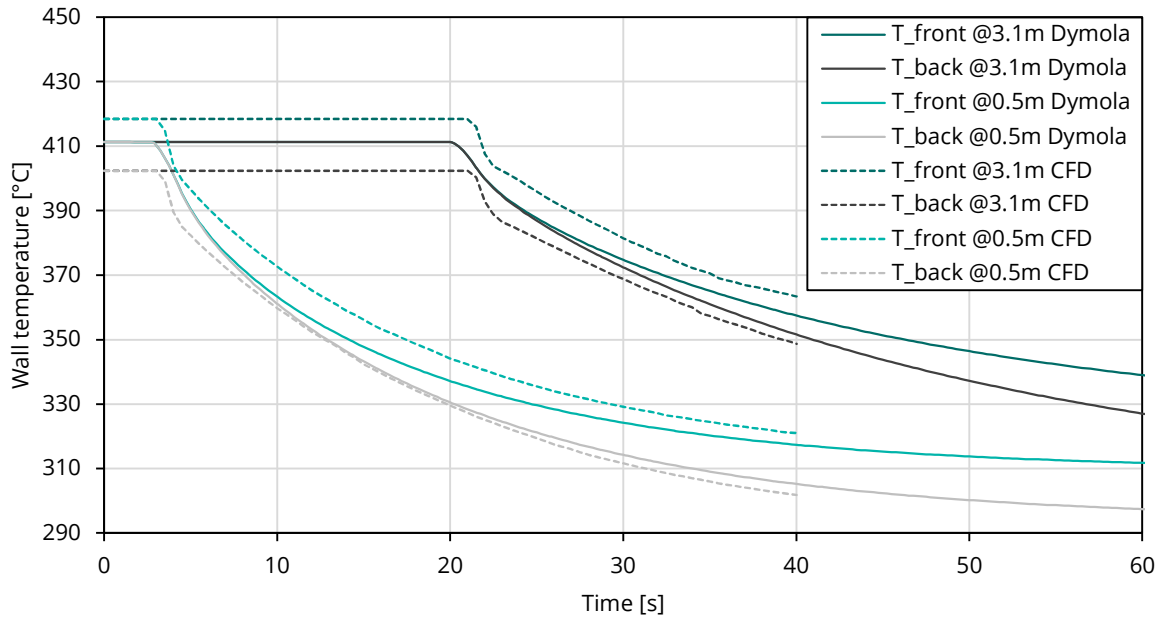
460 Fig. 8. Wall temperature trends during filling at two different heights

4   Simulation Results

4.1   Startup Simulation

463 The following section discusses the simulation results of two different startup scenarios focusing on
464 the west oriented receiver flow path. Both scenarios are set on March 21 at -28.298 ° latitude. In
465 scenario 1 the simulation starts at 06:00 (solar time) and the startup begins as soon as sufficient
466 irradiation is available (here after approx. 5 min simulation time). First, the preheat flux densities rise
467 due to increasing sun elevation (compare Fig. 9). The preheat controller continuously determines a
468 floating set point for the flux density on each panel to maintain the desired temperature ramp of
469 approx. 20 K/min. As soon as the available flux density exceeds this set point (after approx. 8.5 min
470 simulation time), the flux density is then limited by the field control system. Consequently, the tube
471 wall temperatures rise gradually as it can be observed in Fig. 10 for six exemplary panels. The back
472 wall temperatures are taken as the measurement signals for the control system. As soon as they all
473 exceed the set point of 290 °C, the preheat flux is ramped down to maintain this temperature (at
474 around 22 min simulation time).

475 In order to prevent tube damage due to high thermal stresses, the transitions between states of
476 operation need to be appropriately smooth to ensure moderate local and temporal gradients in the
477 absorber tubes as well as the welded joints to the headers. The highest temperature transients
478 (temporal gradients) occur on the outer surface on the front side of the radiated absorber tubes. A

look at Fig. 11 reveals that during preheat these transients reach up to approx. 0.7 K/s with a distinctive peak at the same time, when the flux reaches the aforementioned set point for the first time (at around 8.5 min simulation time). In contrast, the header wall experiences a nearly constant temperature rise due to the well-controlled electrical heating.
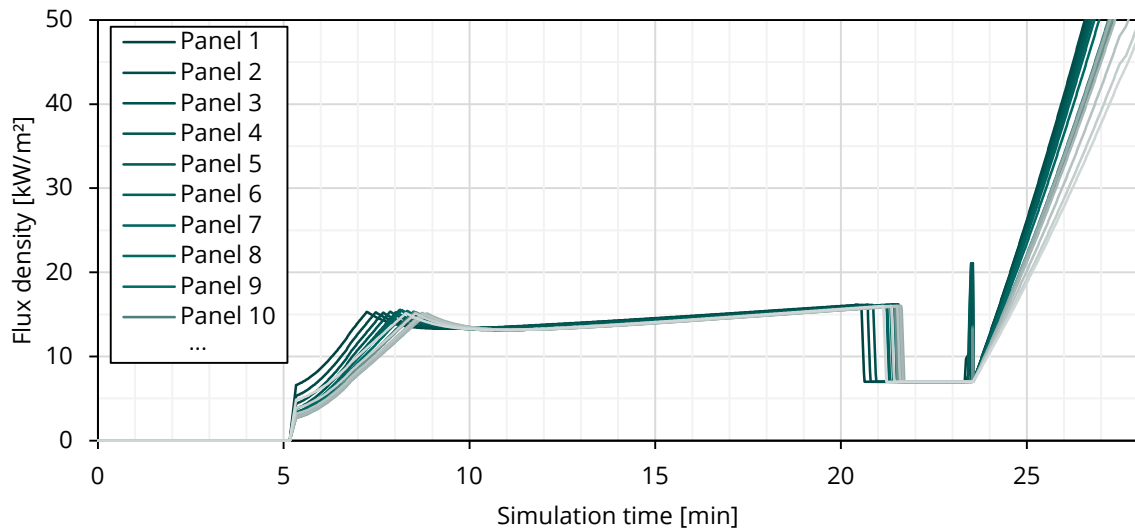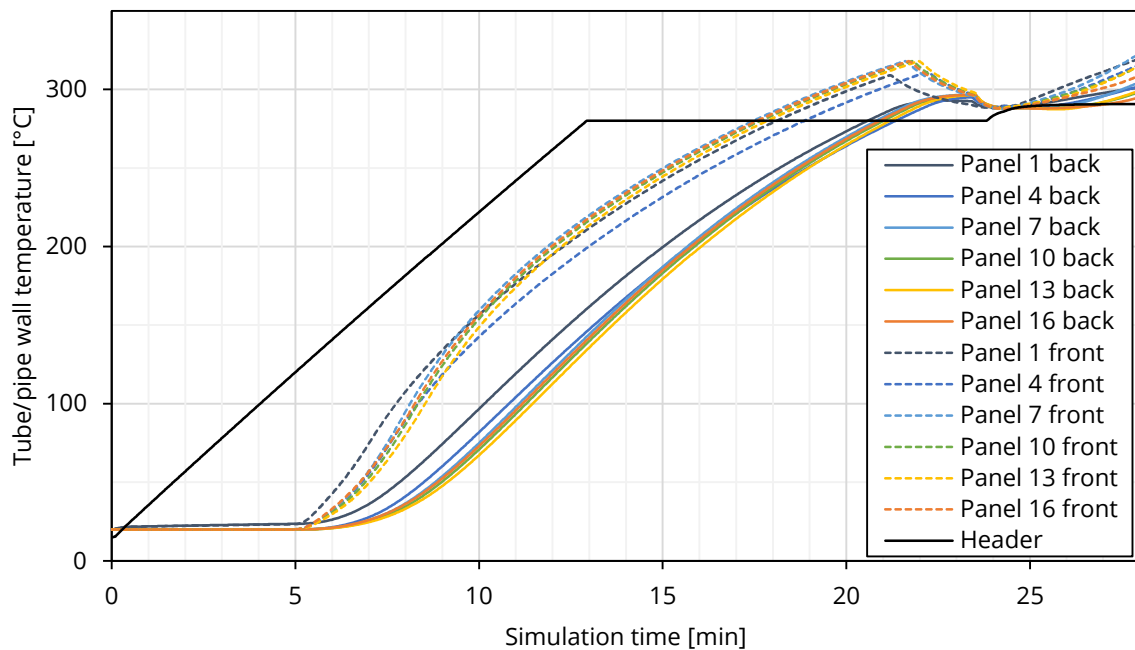
Fig. 9. Flux density trends during preheat and flood

Fig. 10. Temperature trends during preheat in absorber front and back shell elements as well as header wall
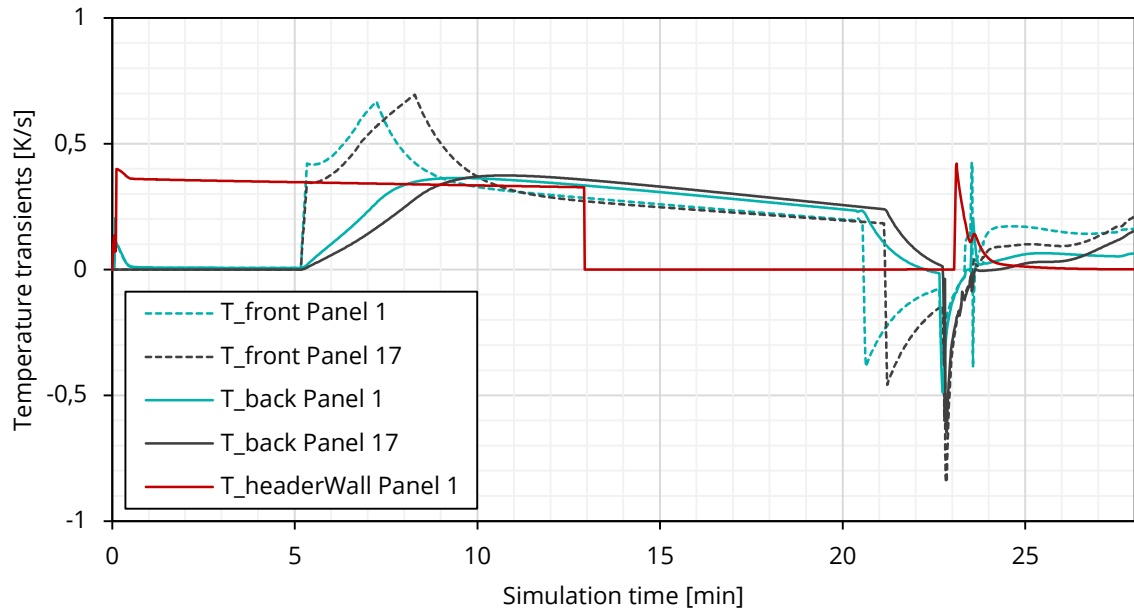
Fig. 11. Temperature transients during startup

After successfully preheating the receiver flood is initialized, recognizable by sudden changes in mass flow rates in Fig. 12 and a peak in temperature transients in Fig. 11 (at approx. 23 min simulation time). The receiver inlet flow is stepped up and thereafter the flow is changed from bypass flow to flood as recognizable by the drain valve mass flow rate (dashed line). This must be compensated by the pumps and the downcomer control valve to maintain acceptable levels, which explains the large variation.
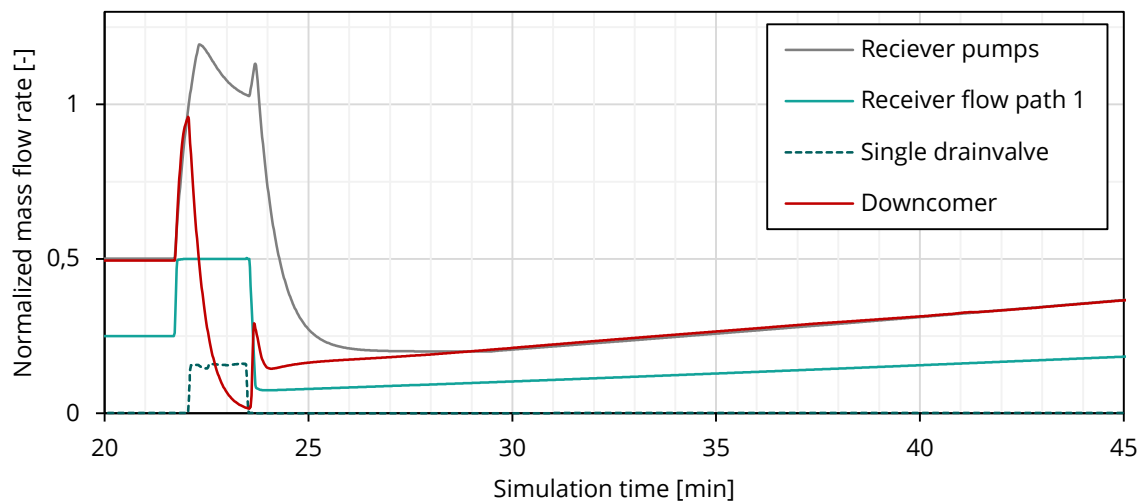
Fig. 12. Mass flow rates in the receiver system during flood

After flooding is completed (at approx. 23.5 min simulation time), the ramp-up procedure is simulated as a linear transition between preheat flux distribution and operational flux distribution, i.e. from a semi homogeneous to a more focused flux. As a result, Fig. 13 shows a smooth temperature transition up to the nominal set value. The flux ramp is configured so that the temperature transients lie in the same range as during preheat. The small peaks that can be noticed

503 in Fig. 14 at 32.5 and 37.5 min are caused by rapid changes of the aim point configuration every five
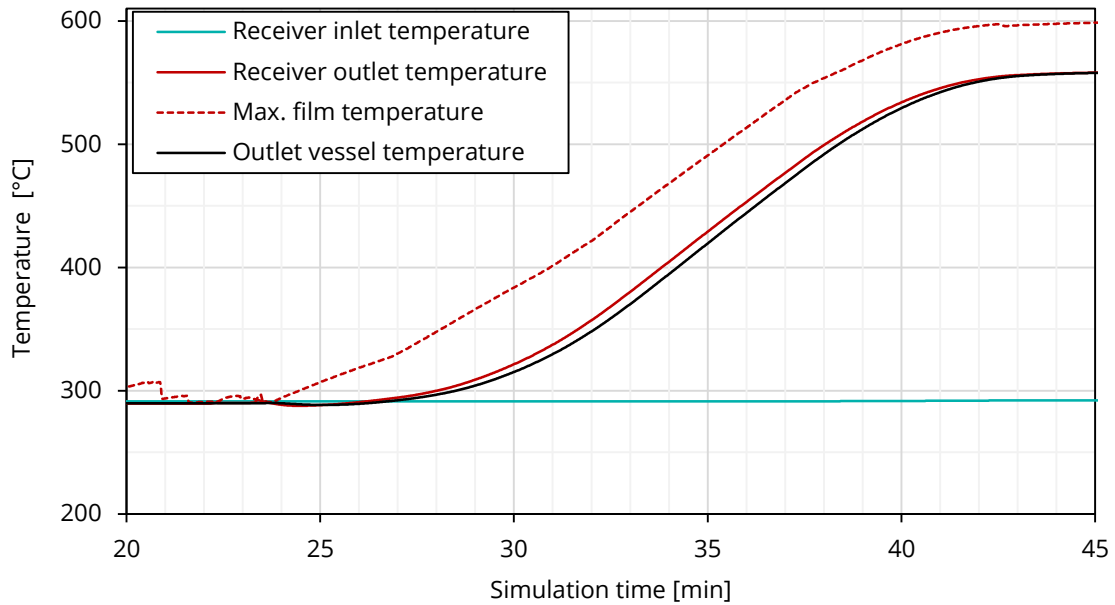504 minutes, which would be smoother in real operation.

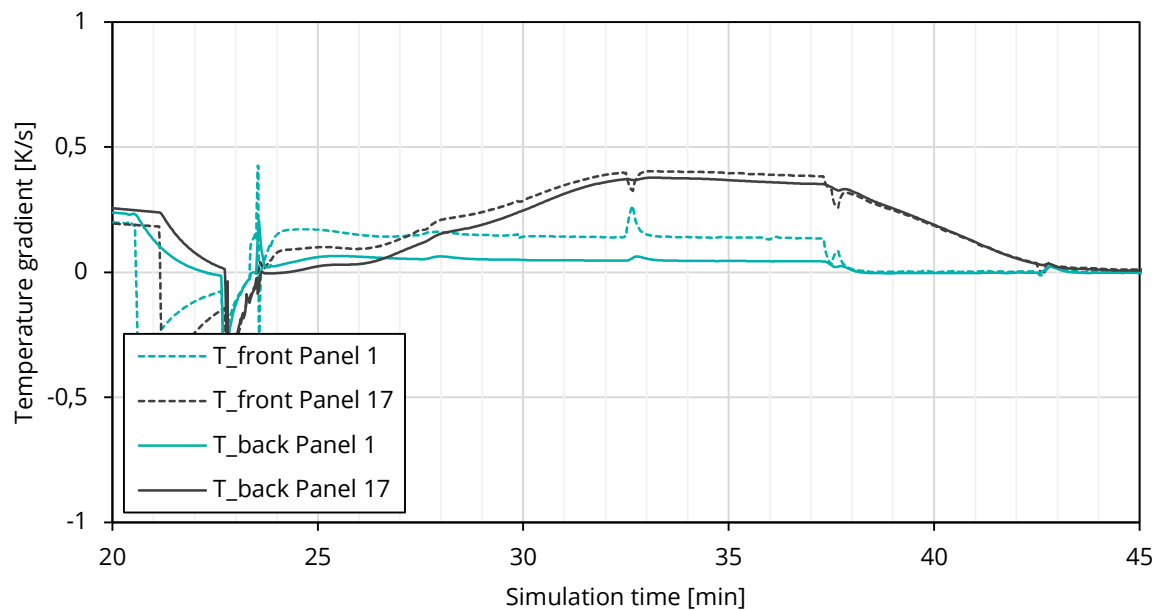506 Fig. 13. Temperature trends during the rampup procedure

509 Fig. 14. Temperature transients during the rampup procedure

511 In summary, until the outlet temperature exceeds the threshold for feeding into the hot storage
512 tank, this early startup takes approx. 39 min, of which 5 min account for waiting until sunrise and can
513 therefore be minimized to the response time of the pumps.

514 In comparison, figure Fig. 15 shows the quick startup in scenario 2 initiating at noon. Due to the
515 higher flux availability, the solar preheat takes 9 min less than in scenario 1, with higher initial
516 temperature transients but still within 1 K/s range. Also, the (filled) temperature ramp-up takes 3 min
517 less due to the higher mass flow rate and therefore a quicker thermal responsiveness of the receiver.
518 Accordingly, the startup duration is 31 min, around 21 % shorter than in scenario 1.

519
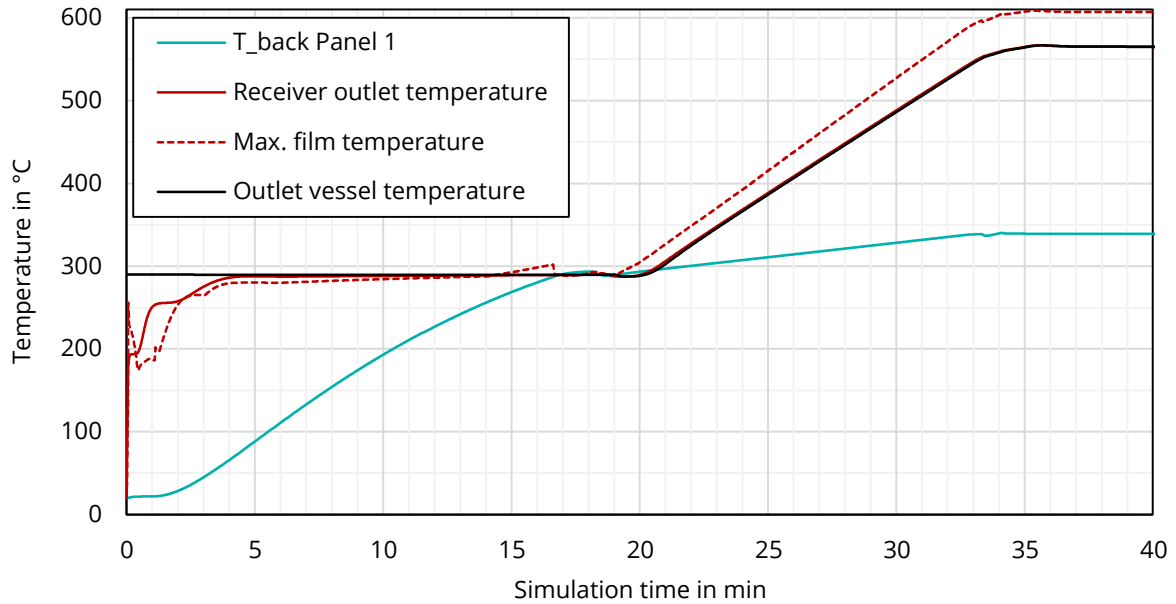
520   Fig. 15. Temperature trends during startup at high flux

4.2 Simulation Performance

522 Thanks to the simplified homogeneous 2P flow modelling approach and in contrast to the former
523 two-fluid modelling approach, this novel 2P receiver tube model offers sufficient numerical stability
524 to allow for transient simulations of the entire receiver system in the two-phase regime. Extensive
525 model optimization on all levels led to satisfactory computing times as well. As illustrated in Fig. 1,
526 the computing time for the above presented validation case of flooding a preheated single receiver
527 tube, in which the preheating takes 3000 s and the flooding 43.3 s simulation time, varies over
528 several orders of magnitude depending on the chosen level of discretization. These tests were
529 carried out on a 2.3 GHz IntelXeon® processor without multithreading but with sparse solver
530 activation in Dymola. As expected, the computing time for the preheating sequence is significantly
531 shorter and increases almost linearly with the number of discrete elements. In contrast, the
532 computational effort for the relatively short filling sequence is much higher and scales approx. by the
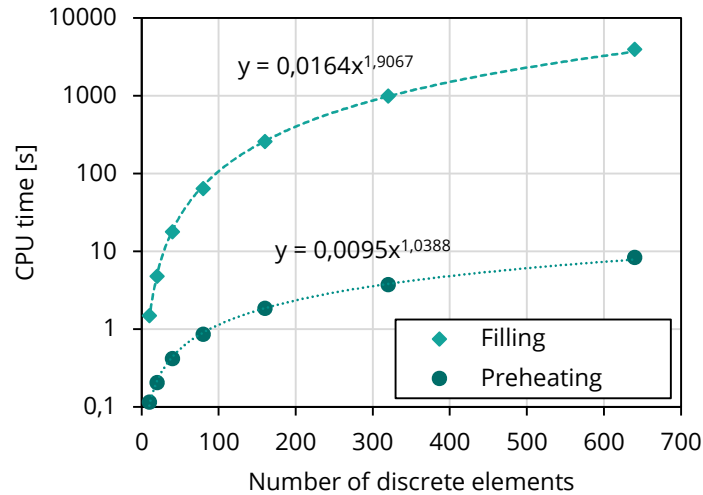533 power of 1.9.

Fig. 16. Required computing time for single tube filling simulation in dependence of chosen discretization

Furthermore, Fig. 17 reveals grid dependencies of the most relevant variables. With only 10 vertical elements, the peak value of the wall temperature transients caused by a sudden change in solar flux is underestimated by more than 18 % and this deviation decreases quickly with higher discretization. But the corresponding bulk temperature transient, which affects especially the downstream components (e.g. headers, outlet vessel), does not show any significant grid dependency. Regarding actual temperatures values the discretization has only a minor effect. The maximum of the molten salt film temperatures in the tube deviates at most by 1.3 K and the outlet temperature by 0.5 K in the investigated range from 10 to 640 vertical elements.
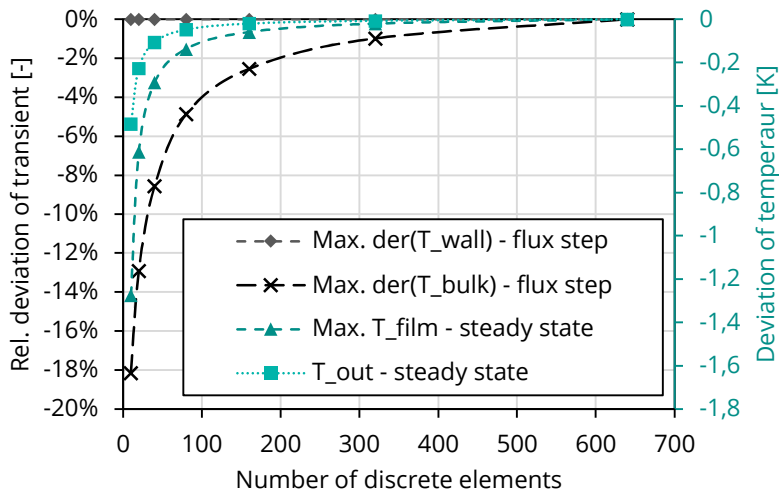

Fig. 17. Grid dependencies of wall temperature transients during filling and film temperatures at normal mass flow

In simulations of the entire system (as in section 2.6) usually a relatively low discretization is chosen to counteract for the added complexity. Fig. 18 shows the computing performance of the startup scenario from section 4.1 with one flow path and 6 vertical tube elements. The total 45 min startup simulation only takes 16.5 min, but as indicated by the red graph, most of the calculation time is spent solving the flood sequence. The cause for this lies in the dynamic integration solver, which on one hand can simulate very efficiently with quite large time intervals (here up to 152 s), but on the other hand, when transients are high, the solver needs to decrease the time step size drastically in order to keep integration errors within the prescribed tolerance. As depicted by the green dots in Fig.

23

555　18, the dynamics during receiver flooding cause the step size of simulation time to drop down into
556　the nanosecond scale. Consequently, the relative CPU time, i.e. computing time per simulation time
557　step, peaks at up to 21, but decreases to almost zero in times with slacker transients. In total, the
558　computation of the startup takes about 37 % of the simulation time.
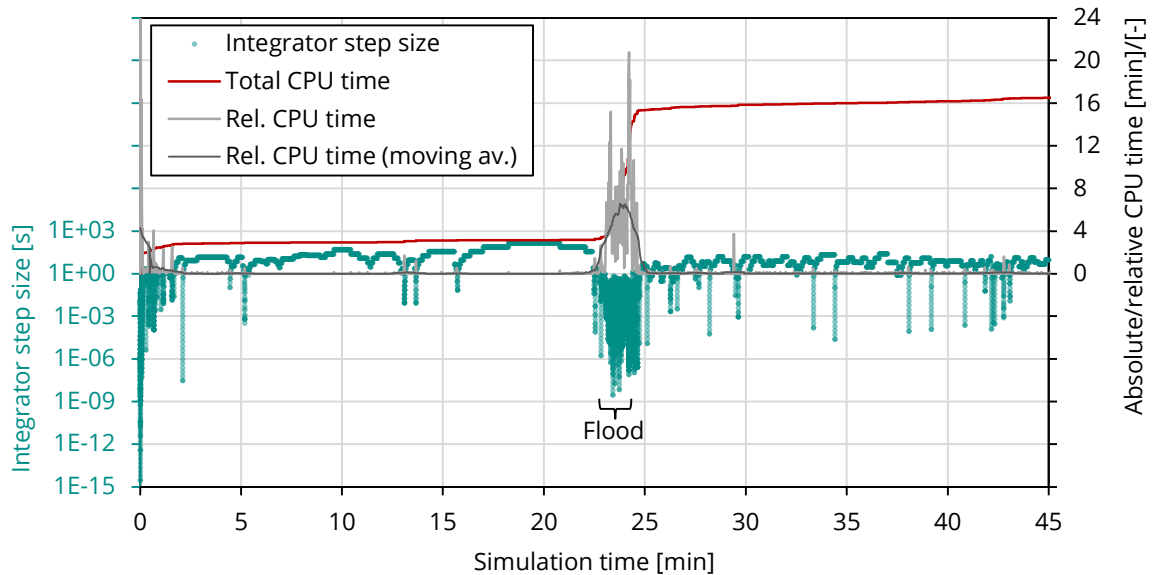

559

560　Fig. 18. Numerical performance during startup simulation, i.e. integrator step size, total CPU time consumption,
561　relative CPU time per simulation time and a corresponding moving average (over 60 s)

5 Conclusion and Outlook

563　A novel modelling approach for transient simulation of a molten salt receiver system has been
564　developed and presented. For an appropriate representation of locally distributed dynamic effects
565　during transitions, while maintaining manageable computing time, a simplified homogeneous two-
566　phase model has been developed and successfully validated for absorber tubes and internal piping.
567　The composed receiver model represents detailed flow characteristics as well as local temperature
568　distributions during normal operation and transitions. Combined with simpler models for peripheral
569　components, the entire receiver system of an MST including thermal storage as well as all necessary
570　local controllers and a process control system is implemented in Modelica Dymola®. Coupling with
571　the raytracing tool STRAL enables simulation with transient flux density distributions.

572　The validation shows good alignment with results from high resolution CFD simulations in steady
573　state operation as well as in transient tube filling, despite the simplified approach of the
574　homogeneous model compared to the previous two-fluid model. However, the two-fluid model was
575　numerically unstable making it useless for simulating multiple receiver panels. The homogeneous
576　modelling approach made it possible to simulate the whole receiver combined with periphery and a
577　process control system in reasonable time. This enables overall system simulation of the entire
578　startup procedure obtaining results on how the implemented control system is able to keep
579　temperature transients within allowable limits and startup durations depending on different ambient
580　conditions. The simulation of a 45 min long startup procedure takes approx. 16.5 min achieving a
581　computing time to simulation time ratio of 37 %. However, the flooding itself causes most of the
582　computational effort, where this ratio shortly rises above 200 %.

583　Ongoing research focuses on daily simulations in cloudy conditions with drainage and refill
584　maneuvers in respect to the corresponding net yield and how this can be optimized by operational

decisions. The presented simulation model serves as a basis for simplified / specialized process prediction models for an operating assistance system. This shall support the operator's decision making by showing precise predictions based on fast models and algorithms in order to increase availability and actual yield in daily operation.

Acknowledgement

6 References

Ahlbrink, N., Belhomme, B., Flesch, R., Quinto, D.M., Rong, A., Schwarzbözl, P., 2012. STRAL. Fast Ray Tracing Software With Tool Coupling Capabilities for High-Precision Simulations of Solar Thermal Power Plants, in: Proceedings of the SolarPACES Conference 2012.

Ahmadi, M.H., Ghazvini, M., Sadeghzadeh, M., Alhuyi Nazari, M., Kumar, R., Naeimi, A., Ming, T., 2018. Solar power technology for electricity generation: A critical review. Energy Sci Eng 6 (5), 340–361.

Akselsen, A.H., 2012. Simulation of Unstable Two-phase Flows in Long Risers, 112 pp.

Augsburger, G., Favrat, D., 2013. Modelling of the receiver transient flux distribution due to cloud passages on a solar tower thermal power plant. Solar Energy 87, 42–52.

Bauer, O., 1999. Modelling of Two-Phase Flows with Modelica. Master thesis, Lund, Sweden, 100 pp.

Belhomme, B., Pitz-Paal, R., Schwarzbözl, P., 2013. Optimization of Heliostat Aim Point Selection for Central Receiver Systems Based on the Ant Colony Optimization Metaheuristic. J. Sol. Energy Eng 136 (1).

Belhomme, B., Pitz-Paal, R., Schwarzbözl, P., Ulmer, S., 2009. A New Fast Ray Tracing Tool for High-Precision Simulation of Heliostat Fields. Journal of Solar Energy Engineering 131 (3), 031002-031002-8.

Brennen, C.E., 2005. Fundamentals of Multiphase Flow. Cambridge University Press, Cambridge, 410 pp.

Burgaleta, J.I., Ternero, A., Vindel, D., Salbidegoitia, I., Azcarrraga, G., 2012. Gemasolar, Key Points for the Operation of the Plant, in: Proceedings of the SolarPACES Conference 2012.

Crespi, F., Toscani, A., Zani, P., Sánchez, D., Manzolini, G., 2018. Effect of passing clouds on the dynamic performance of a CSP tower receiver with molten salt heat storage. Applied Energy 229, 224–235.

Das, A.K., Iñigo, P., Terdalkar, R.J., Joshi, A., Wang, C., Clark, M.M., McGrane, D., Deng, L., 2015. Design Features and Control Concepts of ALSTOM Molten Salt Receiver. Energy Procedia 69, 350–359.

Doupis, D., Wang, C., Carcorze-Soto, J., Chen, Y.-M., Maggi, A., Losito, M., Clark, M., 2016. Transient simulation of molten salt central receiver. AIP Conference Proceedings 1734 (1), 30013.

Flesch, R., Frantz, C., Maldonado Quinto, D., Schwarzbözl, P., 2017. Towards an optimal aiming for molten salt power towers. Solar Energy 155, 1273–1281.

Flesch, R., Högemann, D., Hackmann, J.M., Uhlig, R., Schwarzbözl, P., Augsburger, G., Clark, M., 2016. Dynamic modeling of molten salt power towers, in: Proceedings of the SolarPACES Conference 2016.

Flesch, R., Maldonado, D., Schwarzbözl, P., 2018. Dynamic Modelling of Molten Salt Central Receiver Systems, in: , 9th Mathmod Conference 2018.

Francke, H., 2014. Thermo-hydraulic model of the two-phase flow in the brine circuit of a geothermal power plant [PhD thesis], 152 pp.

Fritsch, A., Uhlig, R., Marocco, L., Frantz, C., Flesch, R., Hoffschmidt, B., 2017. A comparison between transient CFD and FEM simulations of solar central receiver tubes using molten salt and liquid metals. Solar Energy 155, 259–266.

García, E., Calvo, R., 2012. One Year Operation Experience of Gemasolar Plant, in: Proceedings of the SolarPACES Conference 2012.

García, J., Soo Too, Y.C., Padilla, R.V., Beath, A., Kim, J.-S., Sanjuan, M.E., 2018. Dynamic performance of an aiming control methodology for solar central receivers due to cloud disturbances. Renewable Energy 121, 355–367.

Hoffmann, A., Merk, B., Hirsch, T., Pitz-Paal, R., 2014. Simulation of thermal fluid dynamics in parabolic trough receiver tubes with direct steam generation using the computer code ATHLET. Kerntechnik 79 (3), 175–186.

Issa, R.I., Kempf, M.H.W., 2003. Simulation of slug flow in horizontal and nearly horizontal pipes with the two-fluid model. International Journal of Multiphase Flow 29 (1), 69–95.

Kolb, G.J., 2011. An Evaluation of Possible Next-Generation High-Temperature Molten-Salt Power Towers. Sandia National Laboratories, Albuquerque, New Mexico.

Li, Z., Wang, Z., Zhang, Q., Bai, F., 2019. A fast molten salt receiver model in MATLAB. AIP Conference Proceedings 2126 (1), 30034.

Losito, M., Maggi, A., Sani, A., Flesch, R., Schwarzbözl, P., 2018. Dynamic analysis of extraordinary operations of molten salt central receiver. AIP Conference Proceedings 2033 (1), 210008.

Masella, J.M., Tran, Q.H., Ferre, D., Pauchon, C., 1998. Transient simulation of two-phase flows in pipes. International Journal of Multiphase Flow 24 (5), 739–755.

Mehos, M., Price, H., Cable, R., Kearney, D., Kelly, B., Kolb, G., Morse, F., 2020. Concentrating Solar Power Best Practices Study. National Renewable Energy Laboratory (NREL).

Montoya, A., Rodríguez-Sánchez, M.R., López-Puente, J., Santana, D., 2019. Thermal stress variation in a solar central receiver during daily operation. AIP Conference Proceedings 2126 (1), 30038.

Oberkirsch, L., Maldonado Quinto, D., Schwarzbözl, P., Hoffschmidt, B., 2021. GPU-based aim point optimization for solar tower power plants. Solar Energy 220, 1089–1098.

Pacheco, J.E., Bradshaw, R.W., Dawson, D.B., De la Rosa, W., Gilbert, R., Goods, S.H., Hale, M.J., Jacobs, P., Jones, S.A., Kolb, G.J., Prairie, M.R., Reilly, H.E., Showalter, S.K., Vant-Hull, L.L., 2002. Final Test and Evaluation Results from the Solar Two Project. Sandia National Laboratories, Albuquerque, New Mexico.

661 Popp, R., Iding, K., Schwarzbözl, P., Konrad, T., Abel, D., 2021. A Comparison Between Model
662   Predictive and PID-Based Control of a Molten Salt Solar Tower Receiver, in: , SolarPACES
663   Conference 2021.

664 R. Popp, R. Flesch, T. Konrad, U. Jassmann, D. Abel, 2019. Control-Oriented Model of a Molten Salt
665   Solar Power Central Receiver, in: 2019 18th European Control Conference (ECC), pp. 2295–2300.

666 Relloso, S., 2019. Noor III 150 MW Molten Salt Tower: 1st Year of Commercial Operation, 1 October
667   2019, Casablanca.

668 Relloso, S., García, E., 2015. Tower technology cost reduction approach after Gemasolar experience.
669   Energy Procedia 69, 1660–1666.

670 Relloso, S., Gutiérrez, Y., 2016. SENER molten salt tower technology. Ouarzazate NOOR III case,
671   in: Proceedings of the SolarPACES Conference 2016.

672 Rodriguez-Sanchez, M.R., Sanchez-Gonzalez, A., Marugan-Cruz, C., Santana, D., 2015. Flow patterns
673   of external solar receivers. Solar Energy 122, 940–953.

674 Sánchez-González, A., Rodríguez-Sánchez, M.R., Santana, D., 2020. Allowable solar flux densities for
675   molten-salt receivers: Input to the aiming strategy. Results in Engineering 5, 100074.

676 Sani, A., Maggi, A., Losito, M., 2018. 24h dynamic simulation of a CSP solar tower demo plant. AIP
677   Conference Proceedings 2033 (1), 210016.

678 Scheuerer, M., Scheuerer, G., 1992. Two-Fluid Model Simulation of Two-Phase Flow Problems Using a
679   Conservative Finite-Volume Method 1992, 310–315.

680 Schöttl, P., Bern, G., van Rooyen, D.W., Flesch, J., Fluri, T., Nitz, P., 2018. Efficient modeling of
681   variable solar flux distribution on Solar Tower receivers by interpolation of few discrete
682   representations. Solar Energy 160, 43–55.

683 Schwager, C., Boura, C.J.T., Flesch, R., Alexopoulos, S., Herrmann, U., 2019. Improved efficiency
684   prediction of a molten salt receiver based on dynamic cloud passage simulation. AIP Conference
685   Proceedings 2126 (1), 30054.

686 Uhlig, R., Frantz, C., Flesch, R., Fritsch, A., 2018. Stress analysis of external molten salt receiver. AIP
687   Conference Proceedings 2033 (1), 40040.

688 van Zwieten, J.S.B., Sanderse, B., Hendrix, M.H.W., Vuik, C., Henkes, R.A.W.M., 2015. Efficient
689   Simulation of One-Dimensional Two-Phase Flow with a New High-Order Discontinuous Galerkin
690   Method, 43 pp.

691 Vant-Hull, L.L., 2002. The Role of "Allowable Flux Density" in the Design and Operation of Molten-Salt
692   Solar Central Receivers. J. Sol. Energy Eng 124 (2), 165–169.

693 Verein Deutscher Ingenieure, V., 2013. VDI-Wärmeatlas. Springer Vieweg, 2013. 11., bearb. und erw.
694   Aufl, Berlin.

695 Vij, A.K., Dunn, W.E., 1996. Modeling of Two-Phase Flows in Horizontal Tubes, 127 pp.

696 Zavoico, A.B., 2001. Solar Power Tower - Design Basis Document, San Francisco.